# Activation-pathway transitions in human voltage-gated proton channels revealed by a non-canonical fluorescent amino acid.

Esteban Suárez-Delgado[1,2], Gisela E. Rangel-Yescas[1] and León D. Islas[1*]

From:

[1]Department of Physiology, School of Medicine, UNAM, Mexico City,04510, Mexico

[2]Current affiliation: Department of Biology, Xenon Pharmaceuticals Inc., 3650 Gilmore Way, Burnaby, BC V5G 4W8, Canada

*Correspondence to:

León D. Islas

Department of Physiology

School of Medicine

Universidad Nacional Autónoma de México (UNAM)

Circuito Escolar S/N, Ciudad Universitaria

Ciudad de México, 04510, México

leon.islas@gmail.com

ORCIDs

E. Suárez-Delgado: https://orcid.org/0000-0003-0147-3451

G. Rangel-Yescas: https://orcid.org/0000-0003-2766-6040

L.D. Islas: https://orcid.org/0000-0002-7461-5214

## Significance statement

The activation mechanisms of voltage-gated proton channels ($H_V1$) are not well understood. Here we have combined patch-clamp fluorometry and a fluorescent non-canonical amino acid to uncover transitions in the activation pathway of human $H_V1$ that are modulated by voltage and the pH gradient.


## Abstract

Voltage-dependent gating of the voltage-gated proton channels ($H_V1$) remains poorly understood, partly because of the difficulty of obtaining direct measurements of voltage sensor movement in the form of gating currents. To circumvent this problem, we have implemented patch-clamp fluorometry in combination with the incorporation of the fluorescent non-canonical amino acid Anap to monitor channel opening and movement of the S4 segment. Simultaneous recording of currents and fluorescence signals allows for direct correlation of these parameters and investigation of their dependance on voltage and the pH gradient (ΔpH). We present data that indicate that Anap incorporated in the S4 helix is quenched by an aromatic residue located in the S2 helix and that motion of the S4 relative to this quencher is responsible for fluorescence increases upon depolarization. The kinetics of the fluorescence signal reveals the existence of a very slow transition in the activation pathway, which seems to be singularly regulated by ΔpH. Our experiments also suggest that the voltage sensor can move after channel opening and that the absolute value of the pH can influence the channel opening step. These results shed light on the complexities of voltage-dependent opening of human $H_V1$ channels.


## Introduction

Voltage-gated, proton-permeable ion currents in a large variety of cell types and organisms are produced by the $H_V1$ gene (HVCN1 in humans), which encodes a membrane protein that is a member of the superfamily of voltage-sensing domains (VSDs) (1, 2). These VSDs are encountered in voltage-sensitive phosphatases (VSP) and voltage-gated ion channels (VGIC), and their principal function is to detect the membrane potential difference and translate it into a conformational change that activates VSP and opens VGIC (3).

$H_V1$ is thought to form ion channels activated by voltage and employing a mechanism of activation similar to the VSDs of canonical voltage-gated potassium, sodium and calcium channels (4). The functions of $H_V1$ channels are diverse, including intracellular pH regulation (5), charge compensation during immune response (6), modulation of flagellar beating in spermatozoa (7), bioluminescence (8), and possible roles in calcification processes in marine organisms (9, 10). Also, $H_V1$ is involved in different pathologies such as B cell malignancy (11), breast cancer (12), and post-ischemic brain injury (13, 14); consequently, in recent years $H_V1$ has emerged as a possible pharmacological target (15, 16).

Among all voltage-gated proton channels sequenced, the human orthologue, $hH_V1$, is the most widely studied (17). This channel is thought to be a functional dimer formed by two subunits comprising an intracellular N-terminus, a bundle of four transmembrane helices (TMH, S1-S4) in the VSD fold, and a long intracellular alpha helix that mediates a coiled-coil interaction, mainly responsible for dimerization and cooperative activation (18–20). The fourth alpha helix, S4, contains positive charges represented by three arginine residues (R205, R208, and R211) in the characteristic VSD repeats and is thought to undergo an outward displacement and rotation in response to depolarization, mostly in accordance to the helical screw rotation and displacement model of voltage-gating (21). Unlike canonical VGIC, $H_V1$ lacks the two TMH that make up the pore region in canonical ion channels (S5 and S6); therefore, the VSD of $H_V1$ has a double function: it is responsible for detecting the electrical potential across the membrane and forming the pathway through which the protons will move once the channel is activated.

A characteristic of $H_V1$ activation is its dependence on the pH gradient or ΔpH ($pH_o$ - $pH_i$). Native proton channels were first shown to open at more negative voltages when the proton gradient points in the outward direction (22). It was shown that for every unit of ΔpH, the voltage of mid activation shifts ~40 mV. Subsequently, all native and cloned proton channels have been found to approximately follow this rule (1, 2, 10, 17, 23, 24). Recent experiments suggest that the proton gradient produces this effect by acting on the voltage sensor and not only affecting a close-to-open transition, since gating currents and channel opening are similarly modulated (25, 26). However, the molecular mechanisms through which protons modulate voltage-sensor function are not known. Due to technical

difficulties, such as not having a pore structure separate from VSD or the impossibility of patch-clamping without protons in the experiments, gating current recordings of $H_V1$ channels have been obtained from mutants of the *Ciona* $H_V1$ (ci$H_V1$) orthologue (26, 27) or mutants of human $H_V1$ (28).

Patch-clamp Fluorometry (PCF) is a powerful tool that allows investigation of electrically silent conformational changes in VSDs associated with channel gating (29). In ci$H_V1$, this technique has been used to obtain evidence of cooperative gating, S1 movement, and the pH sensitivity S4 movement (25, 30, 31). Here, we assess the conformational changes of the S4 from the human voltage-gated proton channel in response to voltage activation and pH modulation with a genetically encoded fluorescent non-canonical amino acid, Anap, of similar size to aromatic amino acids, and a fluorescent signal with strong stability to acidity changes. We find our measurements can resolve a transition during the deactivation process that is strongly modulated by pH. Furthermore, we find that the changes in Anap fluorescence could be produced by the presence of aromatic amino acids within $H_V1$.

## Results

### *Incorporation of Anap into h$H_V1$*

To study voltage-dependent transitions in a voltage sensor using patch-clamp fluorometry, it's desirable that the introduced fluorescent probe does not produce a major structural perturbation of the target protein. The relatively recently developed probe Anap (3-(6-acetylnaphtalen-2-ylamino)-2-aminopropanoic acid) is a small non-canonical fluorescent amino acid (Figure 1B) which has been shown to be easily genetically-encoded in proteins expressed in eukaryotic cells (32, 33) and useful as a reporter of voltage-dependent conformational changes (34) and as a FRET pair (35) to probe ion channel dynamics. In this study Anap was inserted into specific positions of the S4 segment of the human $H_V1$ proton channel (h$H_V1$) sequence (Figure 1A), with the purpose of examining its voltage and pH-dependent dynamics.

We selected the S4 helix as insertion target, since this region of the channel is proposed to undergo a voltage-dependent outward displacement that has been previously studied with different approaches, including voltage-clamp fluorometry (13–15).

125 Anap efficiently rescued expression of channels containing an amber stop codon (TAG) in
126 the indicated position, as judged both by appearance of red fluorescence produced by the
127 mCherry fluorescent protein appended in the C-terminus or the appearance of proton
128 currents recorded from HEK 293 cells in the whole-cell patch-clamp configuration (Figure
129 1C and Supplementary figure 1).
130 We were able to successfully substitute amino acids by Anap at positions Q191, A197,
131 L198, G199, L200, L201 and I202 in the S4. The substituted channels gave rise to voltage-
132 activated currents, with similar range of activation to WT as judged by their conductance
133 vs. voltage (G-V) curves (except I202Anap channels) (Figure 1D and Supplementary figure
134 2 and Supplementary Table I). The observed fluorescence emission spectrum of the Anap
135 signal present in the membrane (Figure 1C), which presumably originates mostly from
136 Anap incorporated into channels, shows that there are no major or systematic variations
137 on the peak emission wavelength (Figure 1E). The peak emission for all positions is
138 between 480-487 nm, except the most C-terminal and presumably deepest position,
139 I202Anap, which is 479 nm. This result suggests that the local environment of Anap in
140 these positions is very similar and consistent with a polar environment since the peak
141 emission of Anap in aqueous solution is ~486 nm (Supplementary Figure 3C and D). Figure
142 1E also shows that the emission spectra of positions other than Q191Anap exhibit a small
143 extra peak near 610 nm that corresponds to the peak emission of mCherry. Since the 405
144 nm laser used to excite Anap does not excite mCherry, these results suggest that channel-
145 incorporated Anap is able to undergo resonant energy-transfer (FRET) with mCherry. We
146 did not attempt to quantify FRET between Anap and mCherry.
147
148 ***Insensitivity of Anap to pH***
149 In order to use Anap as a reporter of conformational changes in $H_V1$ proton channels and
150 given that these channels are able to change the pH of the surrounding solution (36, 37),
151 we first wanted to validate if this fluorophore is insensitive to pH changes. The amino acid
152 form of Anap that we use is the methyl-ester, which contains amino and carboxy groups,
153 whose protonation could alter the electron distribution and thus its fluorescence, as a
154 function of pH. In fact, the fluorescence of the free form of Anap in solution is highly

155 sensitive to pH, with changes in both the peak emission wavelength and the intensity,
156 presumably reflecting the pKa's of amino and carboxy groups (Supplementary Figure 3E).
157 We reasoned that the best assay to test the pH dependence of Anap fluorescence is to use
158 already incorporated Anap. For this purpose, we used the mutant Q191Anap, which
159 incorporates Anap in the S3-S4 loop which faces the extracellular solution, even in the
160 deactivated state of the channel (Figure 1A). The emission spectrum of Q191Anap channels
161 was measured from transfected HEK cells in which the pH of the extracellular solution was
162 changed over the range 3 to 9.
163 These measurements showed that the fluorescence of Anap is not significantly changed in
164 intensity or shape of the emission spectrum (Figure 2A and B), indicating that this
165 fluorophore is insensitive to pH and that Anap fluorescence should not be affected by pH
166 changes, which might be produced as a consequence of proton currents.
167 As a further test of our data showing pH-insensitivity of channel-incorporated Anap and to
168 validate the use of Anap in proton channels, we incorporated the amino acid in a position at
169 the N-terminus of the channel, V62Anap. This amino acid is located in the intracellular part
170 of the channel and should be subject to changes in local internal pH during channel
171 activation (36) but not show changes in fluorescence as a function of voltage-dependent
172 conformational changes. As expected, we did not detect Anap fluorescence changes,
173 although the amino acid was incorporated into functional channels, as judged from proton
174 currents recorded simultaneously with fluorescence (Figure 2C and D). This result further
175 supports the use of Anap in voltage-gated proton channels to measure conformational
176 changes.
177
178 ***Voltage-dependent changes of Anap fluorescence***
179 Previous experiments in which other dyes like tetra-methyl-rhodamine maleimide (TMRM)
180 were used to label cysteine residues in the S4 segment of voltage-sensing domains,
181 including the *Ciona* and human $H_V1$ channels (25, 30, 31), usually result in fluorescence
182 signals that are reduced upon depolarization by a voltage-dependent quenching process
183 (38, 39). In contrast, when we incorporate Anap at position A197, located towards the
184 extracellular end of the S4, depolarization induced an increase of the fluorescence, along
185 with proton currents. The fluorescence increase saturates at depolarized voltages,

186 suggesting that it is produced by a saturable process such as voltage-sensor activation. The
187 direction of this fluorescence change is the same when measured at a ΔpH of 0 or 2,
188 suggesting the same conformational change in the S4 voltage sensor occurs at different pH
189 gradients, albeit over a different range of voltages (Figure 3A and B). The time course of the
190 fluorescence change is very similar to the time course of proton current activation. The
191 values of the time constants of activation (tau) are very similar, with the fluorescence
192 signal slightly slower, but with comparable voltage dependence (Figure 3C).
193 When F-V and G-V curves are plotted together, it is evident that sensor movement
194 paralleled the activation of the proton conductance. At three different values of the pH
195 gradient (ΔpH 0, 1 and 2), both the F-V and G-V curves are almost superimposable and shift
196 along the voltage axis by the same amount of ~40 mV/pH unit (Figure 3D), which is
197 expected of $H_V1$ channels (22). Only at ΔpH = 2 the fluorescence signal is shifted to slightly
198 more negative voltages than the conductance and only at voltages at which channel
199 activation begins. The observed voltage shift of the G-V is ~31 mV from ΔpH 2 to 1 and ~43
200 mV from ΔpH 1 to 0 and is very similar for the F-V curves. This result indicates that the
201 ΔpH-dependence of gating is preserved in channels with incorporated Anap and that the
202 voltage sensor movement occurs in the same voltage range as the formation of the proton
203 permeation pathway.
204
205 To understand the origin of the increased fluorescence observed during activation, we
206 measured the emission spectra of A197Anap in voltage-clamped cells at different voltages.
207 Figure 3E plots the normalized spectra obtained at voltages ranging from -100 to 140 mV
208 and it shows that the spectra superimpose well, indicating that the increase in fluorescence
209 is not due to depolarization-driven wavelength shifts of the emission spectra. We interpret
210 this result as an indication that Anap incorporated at position A197 remains in a polar
211 environment at all voltages or that small changes in polarity change the quantum yield of
212 Anap but not the emission spectrum.
213
214 ***$H_V$1-197Anap is quenched by a phenylalanine in the S2***

215 The increase of the Anap fluorescence at position 197 in the S4 seen with depolarization
216 could be interpreted as a reflection of an outward movement of the S4 and exposure of
217 Anap to a more polar environment, which in principle will produce a red shift of the
218 emission spectrum and an increase of the fluorescence that is detected. However, as shown
219 in Figure 3E, the shape of emission spectrum of Anap remains unchanged at all voltages
220 and with a constant emission peak at ~480 nm, indicating that the fluorophore remains in
221 a polar environment in the closed and open states and thus, a change in local polarity is not
222 the cause of dequenching.
223 Anap was derived from Prodan (32) and although the photophysical behavior of Anap is
224 not well characterized, Prodan's fluorescence is known to be quenched by mechanisms
225 such as π-stacking or photoinduced electron transfer with aromatic amino acids (40), both
226 mechanisms which require close proximity. For these reasons, it is conceivable that the
227 Anap quencher in $H_V1$, could be an aromatic residue that is located near the introduced
228 fluorophore in the closed state and upon S4 movement, increases its distance, generating
229 the observed dequenching. We used a structural model of $H_V1$ derived from experimental
230 data (41) and replaced A197 with Anap. Figure 4A shows Anap in salmon-colored spheres
231 and highlights aromatic residues within the transmembrane domains of a monomer as
232 dotted spheres. A possible candidate for an Anap quencher is F150 (yellow spheres),
233 because this residue is the closest aromatic to Anap that is not in the S4 and F150 will
234 presumably remain in its position as 197Anap undergoes an outward displacement with
235 depolarization. In contrast, other aromatic residues which are closer to 197Anap and are
236 part of the S4, will presumably move with all the S4 as a rigid body. Incidentally, an
237 equivalent phenylalanine to F150 has been identified as the charge transfer center in
238 canonical voltage-gated potassium channels and in $H_V1$ (42, 43).
239 To test this hypothesis, we made the double mutant F150A-A197Anap and estimated the
240 relative amount of basal Anap quenching, by comparing the emission spectra of both Anap
241 and mCherry in the same membrane region. Figures 4B and C shows that the double
242 mutant displays a significantly increased Anap fluorescence (~60 %) relative to mCherry,
243 when compared to A197Anap alone, suggesting that indeed, phenylalanine 150 is capable

244 of quenching Anap in the closed state (at the resting potential of HEK cells of -20 to -40 mV
245 (44) and at the employed ΔpH ~ -0.2 ($pH_o$ = 7) most channels should be in the closed state).
246 Despite having removed the quenching group, F150A-A197Anap channels still show
247 voltage-dependent fluorescence changes (Figure 4D), suggesting the presence of additional
248 quenchers or that in the absence of F150, Anap at 197 becomes sensitive to polarity
249 changes.
250 The voltage dependence of the fluorescence signals from F150A-A197Anap channels shows
251 significant differences from those of A197Anap alone. At values of ΔpH of 0 and 1,
252 fluorescence precedes the increase in conductance, indicating that the conformational
253 change of the S4 segment occurs at more negative voltages than the formation of the
254 proton-permeable pathway. This effect is more pronounced at ΔpH = 1. Interestingly, the
255 difference of $V_{0.5}$ of the F-V curve between ΔpH= 0 and 1 is 57.8 mV, similar for A197Anap,
256 which is 45.7 mV.
257
258 ***A distinct gating transition detected by Anap fluorescence***
259 The fluorescence time course of the F150A-A197Anap channels shows an interesting
260 characteristic, which is that the OFF signals ($F_{off}$) that are produced at the return of the
261 voltage to the holding potential and represent the return of the voltage sensor to the
262 resting states, show a two-component kinetic behavior. This is particularly evident at ΔpH
263 = 0 (Figure 4D), where $F_{off}$ shows a very rapid quenching followed by a much slower
264 component, suggesting that the voltage sensor can move back to its resting position at
265 varying rates.
266 To explore the kinetics of fluorescence signals, especially during repolarization, and since
267 this double mutant removes a quenching group, we used the $hH_V1$-201Anap channels. We
268 reasoned that this mutant channel, which has Anap in a deeper position in the S4 and
269 presumably closer to F150 in the closed state, might be a better reporter of the kinetics of
270 S4 movement.
271 Figures 5A, B and C show simultaneous current and fluorescence recordings from $hH_V1$-
272 L201Anap channels at three different ΔpH values of 0, 1 and 2. As with the $hH_V1$-A197Anap

construct, the voltage-dependence of the conductance and fluorescence are almost superimposable and shows a large shift of >40 mV/pH unit (Figure 5D).

The most salient feature of these fluorescence traces is that, at ΔpH = 0, the OFF signal during repolarization ($F_{off}$) has two distinct kinetic components. The deactivation tail currents at -60 mV decay exponentially, with a time constant of 141 ± 55 ms, while the $F_{off}$ can be fit to a sum of two exponentials with time constants of 129 ± 68 ms and 8.6 ± 0.74 s. (Supplementary figure 4). The presence of the two components in $F_{off}$ suggest that the return of the voltage sensor to its resting state can occur at varying rates. In particular, the slow component is consistent with the immobilization of the off-gating charge observed in monomeric *Ciona* $H_V1$ channels (27). The slow off-component is also present at ΔpH = 1 and 2, although its amplitude is smaller. The slow return of the voltage sensor at ΔpH = 0 is also consistent with the more positive voltages needed to activate the channel at this pH gradient.

To qualitatively understand the kinetics of the fluorescence signals, we used a simplified kinetic model of channel activation (Scheme I), similar to a model that was previously used to study the voltage-dependent kinetics of $hH_V1$ (45).

$$C_0 \underset{k_{10}}{\overset{k_{01}}{\rightleftharpoons}} C_1 \underset{k_{21}}{\overset{k_{12}}{\rightleftharpoons}} C_2 \underset{k_{32}}{\overset{k_{23}}{\rightleftharpoons}} O_3$$

Scheme I

In this model, one of the backward transitions ($k_{21}$) between closed states is set to be much slower than the open to closed transition ($O_3$->$C_2$), resulting in a large difference between the closing kinetics of the ionic current, mostly determined by $k_{32}$, and the fluorescence signals. This kinetic difference can account for the biphasic behavior of the $F_{off}$ signal, and especially the slow component of its time course (Figure 5D). The model also indicates that when the internal pH is lower than the external pH (ΔpH=2), this slow rate constant is more affected than any other, indicating a conformational step that is especially sensitive to pH.

302 While the simple model in Scheme I can account qualitatively for the observed kinetics of
303 201Anap channels, the experimental F-V relationship is positively shifted by ~10 mV with
304 respect to the G-V curve, which is not a feature of Scheme I and is reminiscent of channels
305 that can open to multiple open states, without the need of full voltage sensor activation
306 (46). This observation suggests that $hH_V1$ channels operate via a more complicated
307 mechanism that the one illustrated by Scheme I, which might include channel opening
308 before complete voltage-sensor movement. We tested a simple version of such an allosteric
309 model and show that it can account, at least qualitatively, for current and fluorescence
310 kinetics and for the relationships between G-V and F-V curves at varying ΔpH
311 (Supplementary figure 5). Interestingly, in this model the slow deactivation rate constant is
312 also the step with the most sensitivity to pH (Supplementary Table III).
313
314 ***Absolute pH values are determinants of voltage sensor movement.***
315 One of the most intriguing characteristics of $H_V1$ channel gating, is its steep modulation by
316 the pH gradient. While it has been shown that this modulation depends on the value of
317 ΔpH, regardless of how it is set up (22), there is evidence that the absolute value of pH can
318 also exert an effect on gating (47). In most of our experiments, the pH gradient was set up
319 with a low value of intracellular pH, between 5.5 and 6. To test the effect of absolute pH, we
320 carried out experiments with the same ΔpH of 0, with symmetric low (5.5/5.5) or high
321 (7/7) intra/extracellular pH. The expectation was that, if pH gating of $hH_V1$ depends only
322 on the pH gradient, the voltage sensor should move with essentially the same
323 characteristics. Surprisingly, the fluorescence signals display important differences, as do
324 the proton currents. Our results in Figure 6 show that when compared to ΔpH of 0
325 (5.5/5.5), the fluorescence in symmetric $pH_o$ and $pH_i$ of 7 has a rapid return of the $F_{off}$
326 signal (Figure 6A and B). Interestingly, the voltage dependence of the F-V relationship is
327 very similar for (5.5/5.5) or (7/7) conditions, while in (7/7) the proton current appears at
328 more positive voltages than the bulk of the fluorescence (Figure 6C).
329 These results suggest that the voltage range of movement of the voltage sensor is
330 dependent on the ΔpH, while the opening of the proton conduction pathway can occur after

331 only a fraction of the voltage sensor movement has occurred and this coupling between
332 voltage sensing and channel opening can be regulated by low pH.
333
334 **Discussion**
335 In the experiments described here we have implemented patch-clamp fluorometry in
336 combination with incorporation of a fluorescent non-canonical amino acid (NCAA) to study
337 voltage-dependent gating in $hH_V1$ proton channels. Although voltage-clamp fluorometry
338 (VCF) has been used previously to study $H_V1$ channels (25, 30, 31), employing the
339 fluorescent Anap NCAA has the advantages of being a smaller size probe and improving the
340 specificity of fluorescence signals, since it is genetically encoded. We were able to
341 incorporate Anap into functional channels in several sites along the S4 and the S3-S4 loop.
342 Since Anap was developed as an environmental sensitive probe, the fact that the emission
343 spectrum of Anap in these sites is very similar to that of Anap in water, suggests that these
344 residues are solvated in the native $H_V1$. The only position that shows a blue-shifted Anap
345 spectrum is I202 which is the most C-terminal residue explored and might burry the Anap
346 R-group in a more hydrophobic environment.
347 Since the activity of $H_V1$ proton channels can change the local concentration of protons
348 near the conduction site and fluorescence probes have been used to detect these proton
349 fluxes (36, 37), we addressed whether Anap could change its fluorescence as a function of
350 pH. We show that Anap is highly insensitive to pH in the range 4 to 8 and it does not change
351 fluorescence in conditions in which high outward fluxes can change the local intracellular
352 pH. Our experiments confirm that Anap can be used without interference from local
353 changes in proton concentration.
354 When incorporated at position 197, Anap produced fluorescence signals that indicate an
355 increase in intensity with depolarization and saturated in magnitude at positive potentials.
356 This behavior indicates dequenching of Anap as the S4 segments undergoes an outward
357 movement during the activation conformational change. Anap has been incorporated in
358 other membrane proteins, including the *Shaker* potassium channel, in which Anap was
359 incorporated in the S4-S5 linker and displayed fluorescence quenching upon depolarization
360 (48). As far as we know, Anap has been incorporated in the S4 of only the
361 hyperpolarization-activated cyclic nucleotide-gated (HCN) channel (49), where it is

362 quenched or dequenched upon hyperpolarization in a position-dependent manner. The
363 direction of the fluorescence changes due to S4 motion are difficult to predict, since, as we
364 have shown, Anap's fluorescence can be affected by both the local environment's polarity
365 and interaction with specific quenching groups that are part of the channel sequence.
366 The fluorescence changes we observe in 197Anap channels indicate that the G-V and F-V
367 relationships have almost the same voltage-dependence at the ΔpH values tested,
368 suggesting that S4 movement closely follows channel opening, and that S4 movement and
369 activation of the proton conductance are equally affected by the proton gradient. A similar
370 conclusion has been reached in studies measuring S4 movements of $hH_V1$ by fluorescence
371 (25) or in *Ciona* $H_V1$ by gating current recordings (26). Interestingly, these changes in
372 fluorescence as a function of voltage, are not accompanied by changes in the emission
373 spectrum of Anap, suggesting that the probe remains in a solvated environment regardless
374 of the state of the channel. This is in accordance with the finding that the VSD that forms
375 $hH_V1$ channels has a large extracellular cavity able to contain many water molecules (50).
376 Since Anap remains solvated in the closed and open state, what is the origin of the reported
377 fluorescence changes? As a Prodan-derived probe, we hypothesized that an aromatic
378 residue could act as an Anap quencher and thus found that the only aromatic outside the S4
379 close enough to have this function is F150. Mutation F150A in the 197Anap background
380 produced an increased Anap/mCherry fluorescence intensity as compared to 197Anap
381 alone, indicating reduced quenching. This result suggests that 197Anap moves away from
382 F150 as the S4 segment moves outward during channel activation.
383 Substitution of L201 for Anap allowed us to uncover a slow step in the activation pathway.
384 The fluorescence signal observed upon channel closure by repolarization at ΔpH = 0 shows
385 two components, one which is much slower than channel closing as reported by the tail
386 current. The fact that tail current is faster than the slow component of the deactivation
387 fluorescence signal indicates that the latter is produced by a slow intermediate transition,
388 as is also recapitulated by a simple kinetic model. Interestingly, recordings of gating
389 currents in mutant *Ciona* $H_V1$ channels show that the charge return after depolarization
390 can be very slow, producing gating charge immobilization (27). This observation of a

391 singular slow transition in $hH_V1$ activation illustrates the value of fluorescence recording
392 with a small probe such as Anap.
393 Our data thus far indicates that a fraction of S4 movement, as reported by the F-V relation,
394 occurs before the increase of the proton conductance, and that S4 movement can continue
395 after channel activation. Comparison of the $V_{0.5}$ values of Q-V and G-V curves in $hH_V1$
396 channels (28) indicates that charge moves at slightly more negative values than
397 conductance, but not at all ΔpH values. Fluorescence changes depend on all the
398 conformational states in which the fluorophore has distinct fluorescence values, while
399 gating currents are produced during transitions between conformations with state-
400 dependent charge distributions (51). For these reasons, F-V and Q-V curves of multistate
401 channels are not expected to be identical or contain the same information.
402 Our fluorescence data are consistent with recent experiments that have shown that the
403 characteristic gating effect of the proton gradient on voltage-gated proton channels comes
404 about by a conformational change that affects voltage sensor movement and not a channel
405 opening transition. Furthermore, our modeling suggests that all transitions in the
406 activation pathway, including a characteristic slow transition detected by fluorescence are
407 modulated by ΔpH.
408 The mechanism of ΔpH modulation is still unknown. It has been proposed that the energy
409 stored in the pH gradient is directly coupled to S4 movement to produce ΔpH-dependent
410 gating (26). We have previously proposed an allosteric model in which both extracellular
411 and intracellular protons can affect local electrostatic networks and bring about ΔpH-
412 gating (10). This class of models predicts the existence of multiple open states, which is
413 supported by the observation that S4 movement can happen after channel opening.
414 A mechanism in which the proton gradient energy is coupled to S4 movement predicts that
415 the absolute value of pH should not influence gating. Interestingly, we have observed that
416 the absolute pH values used to set up a ΔpH = 0 do affect gating. When $pH_o$=5.5/$pH_i$=5.5, G-
417 V and F-V are almost superimposed and the $F_{off}$ signal has a fast and slow component; in
418 contrast, when $pH_o$=7/$pH_i$=7, the F-V curve has almost the same voltage-dependence, but
419 conductance can be observed at more negative voltages and the $F_{off}$ signal only contains the
420 fast component. These results suggest that the absolute pH in the extracellular side of the

421 channel is a determinant of the steady-state gating, presumably modulating the slow rate
422 constant in the activation pathway.
423
424 **Materials and Methods**
425 *Molecular biology and HEK cell expression*
426 A plasmid containing the human voltage-gated proton channel ($hH_V1$) was a gift from Dr.
427 Ian Scott Ramsey (Virginia Commonwealth University, Richmond, VA). We used the
428 fluorescent protein mCherry as a reporter to verify L-Anap incorporation. The construct
429 $hH_V1$-mCherry was made by the PCR overlap technique, adding the sequence of fluorescent
430 protein mCherry after the C-terminus of $hH_V1$ with the following linker sequence: (Gly-Gly-
431 Ser)$_3$. This construct was subcloned into the pCDNA3.1 vector. For all $hH_V1$-TAG mutants,
432 an amber codon (TAG) was introduced using appropriate mutagenic oligonucleotides and a
433 protocol for whole plasmid site-directed mutagenesis employing KOD polymerase (Merck
434 Millipore, Germany) as detailed in manufacturer's instructions and previous work (52, 53).
435 The bacterial methylated DNA templates were digested with the DpnI restriction enzyme,
436 and the mutant plasmids were confirmed by automatic sequencing at the Instituto de
437 Fisiología Celular, UNAM.
438 We used HEK293 cells for channel expression and L-Anap incorporation experiments. The
439 HEK cells used in this study were found free of mycoplasma infection (Sigma-Aldrich
440 mycoplasma detection kit). These cells were cotransfected with 0.1 – 1 μg of mutant $hH_V1$-
441 TAG plasmid and 0.7 μg of pAnap plasmid (a gift from Dr. Sharona Gordon, University of
442 Washington, Seattle, WA) using the transfection reagent JetPei (Polyplus-transfection).
443 The pANAP plasmid contains the orthogonal pair tRNA/aminoacyl tRNA synthetase specific
444 to L-Anap. The Methyl ester form of L-Anap; L-Anap-Me (AsisChem Inc.) was added to the
445 medium of cells in 35 mm culture dishes from a storing stock solution of 10 mM to a final
446 concentration of 10-20 μM. Through the text, we will refer to L-Anap as Anap for simplicity.
447 Cells were incubated during 12-48 hours before experiments in Dulbecco's Modified Eagle
448 Medium (DMEM, Invitrogen) supplemented with 10% fetal bovine serum (Invitrogen, USA)
449 and penicillin-streptomycin (100 units/ml — 100 μg/ml, Invitrogen, USA) at 37 °C in a 5%
450 $CO_2$ atmosphere. Around 4 hours before electrophysiological recordings, HEK293 cells
451 were treated with 0.05% trypsin-ethylenediaminetetraacetic acid (Trypsin-EDTA) to

452 obtain rounded cells, which were then re-platted in 35 mm glass-bottom dishes (World
453 Precision Instruments, USA) and used for experiments within 3-6 hrs. All the experiments
454 were performed at room temperature (~25°C).
455
456 *Electrophysiology*
457 Recordings of proton currents were performed in the whole-cell patch-clamp configuration
458 using fire-polished borosilicate micropipettes (Sutter Instruments, USA). Currents were
459 recorded by an Axoclamp 200B amplifier (Axon Instruments, USA) and acquired with an
460 ITC-18 AD/DA converter (HEKA Elektronik, Germany), both controlled with Patchmaster
461 software (HEKA Elektronik, Germany). Currents were low-passed filtered at 5 kHz and
462 sampled at 20 kHz. The extracellular solution contained (in mM): 100
463 tetramethylammonium hydroxide and methanesulfonic acid (TMAOH-$HMESO_3$), 100 buffer
464 ((2-(N-morpholino)ethanesulfonicacid (MES) for pH 5.5, and 6.0; 4-(2-hydroxyethyl)-1-
465 piperazineethanesulfonic acid (HEPES) for pH 7.0 and 7.5), 2 $CaCl_2$, 2 $MgCl_2$, 8 HCl and pH-
466 adjusted with TMAOH and HMESO. The intracellular solution contained (in mM): 80
467 (TMAOH-$HMESO_3$) 100 buffer (MES for pH 5.5 and 6.0; HEPES for pH 7.0 and 7.5), 10
468 ethylene glycol-bis(β-aminoethyl ether)-N,N,N',N'- tetraacetic acid (EGTA), 10 $MgCl_2$, and 4
469 HCl and pH-adjusted with TMAOH and HMESO. With these solutions, patch pipettes had a
470 resistance of 2-5 MΩ. Since cells used in these experiments were round to improve space-
471 clamp and currents were relatively small, no series-resistance compensation was
472 employed. The voltage-clamp protocols varied depending on the value of ΔpH and are
473 indicated in the figure legends. The interval between each test pulse was 45 s at the holding
474 potential to facilitate return of slow fluorescence signals and minimize the effects of proton
475 depletion.
476
477 *Fluorescence measurements*
478 Fluorescence measurements in whole-cell fluorometry (WCF) experiments were made
479 using a TE-2000U (Nikon, Japan) inverted epifluorescence microscope with a 60x oil
480 immersion objective (numerical aperture 1.4). A 405 nm solid-state laser (Compass 405-50
481 CW, COHERENT, USA) and a filter cube containing a 405/20-nm excitation filter, a 405-nm

482 long pass dichroic mirror, and a 425-nm long-pass emission filter were used for Anap
483 fluorescence excitation. For mCherry fluorescence, measurements were performed using
484 an Ar-Ion laser (Spectra-Physics, Germany) and a filter cube with a 514/10-nm excitation
485 filter, a 514-nm long pass dichroic mirror, and a 530-nm long-pass emission filter (Chroma,
486 USA). Both lasers were through-air coupled, collimated using an optical cage system and
487 appropriate optics (Thorlabs, USA) and then focused into the objective's back focal plane
488 through the microscope's rear port. Imaging was performed using Luca or Ixon Ultra
489 EMCCD cameras (Andor, Oxford instruments, Ireland) controlled by Micromanager
490 software (54). The fluorescence of a region without cells was measured with the same ROI
491 employed with cells and this background was subtracted from Anap fluorescence images.
492 Image stacks from cells were recorded at 10-25 Hz (100 – 40 ms of exposure, respectively).
493 To improve signal-to-noise ratio, 4x4 or 8x8 pixel binning was used. Initially, fluorescence
494 time course was measured from a region of interest (ROI) that included only the membrane
495 of the patched cell. Identical results were obtained by using a ROI encompassing all the cell.

496 Fluorescence and proton current recording synchronization was achieved through a home-
497 programed Arduino Uno microcontroller board (Arduino, Italy) triggered by a
498 PatchMaster-generated TTL pulse.

499 For spectral measurements, the light from the microscope was collected by a SpectraPro
500 2150i imaging spectrograph (Princeton Instruments, USA) mounted between the
501 microscope and EMCCD camera. The spectra of both fluorophores (Anap and mCherry)
502 were recorded by measuring line scans of the spectral image of the cell membrane, and the
503 background fluorescence from a region of the image without cells was subtracted.
504
505 *Data analysis*
506 IgorPro (Wavemetrics) and ImageJ (NIH) software were used to analyze the data. For the
507 G-V relationships, conductance ($G$) was calculated from proton currents according to:

$$G(V) = \frac{I(V)}{V - V_{rev}}$$

508 Where $V_{rev}$ is the proton current reversal potential, measured from the current-voltage
509 relation. Then, $G$ was normalized and fit to a Boltzmann function as follows:

$$\frac{G}{G_{max}} = \frac{1}{1 + \exp^{(q(V - V_{0.5})/K_B T)}}$$

Equation 1

Where $q$ is the apparent gating charge (in elementary charges, $e_0$), $V$ is the membrane potential, $V_{1/5}$ is the potential at which half of the maximal activation is reached, $K_B$ is the Boltzmann constant and $T$ is the temperature in Kelvin.

The time course of fluorescence in WCF experiments, was obtained from all the background-subtracted images in a stack ($F_i$), and the changes through time were normalized to the first image ($F_0$) as follows:

$$\frac{F_i - F_0}{F_0} = \frac{\Delta F}{F_0}$$

Then, this normalization was multiplied by 100 to obtain the percent change of fluorescence. This procedure was carried out for each stack at each voltage. The voltage-dependence of the fluorescence was estimated from F-V relationships. The value of the fluorescence at the end of the volage step was normalized and fit to a Boltzmann function:

$$\frac{F}{F_{max}} = \frac{1}{1 + \exp^{(q(V - V_{0.5})/K_B T)}}$$

Equation 2

Where $F$ is the percent of fluorescence change at $V$ potential and $F_{max}$ is the maximum fluorescence percent change in each experiment at $V$ potential. The meaning of $q$, $V$, $V_{0.5}$ and $K_B T$ is the same as in equation 1. All data are presented as the mean ± standard error of the mean (s.e.m.).

The time constants activation of proton currents and fluorescence signals were obtained by fitting of the second half of each trace to the equation:

$$I \text{ or } F(t) = A_{ss}\left(1 - e^{\left(-(t - t_o)/\tau\right)}\right)$$

Equation 3

Where $A_{ss}$ is the amplitude of the fluorescent signal ($F$) or current ($I$) at steady state, $\tau$ is the time constant, and $t_o$ is the time of start if the voltage pulse, both in ms. The voltage dependence of τ was calculated from a fit to equation:

$$\tau(V) = \tau(0) \cdot e^{\left(\frac{qV}{K_B T}\right)}$$

Equation 4

Where $\tau(0)$ is the activation time constant at 0 mV, $q$ is the partial charge in $e_0$ units and $V$, $K_B$ and $T$ have the same meaning as in equation 1.

*Modelling*

Modelling of current and fluorescence was carried out using custom-written programs in IgorPro (Wavemetrics). The occupancy of each discreet state in the models was calculating by numerically solving the differential equations describing the transitions between states. The occupancy of each discreet state $i$ is $P_i$ and it was calculated by numerically solving the differential equations described by a master equation:

$$\frac{dP_i}{dt} = \sum_{i \neq j} (P_j k_{ji} - P_i k_{ij})$$

The rate constants $k_{ij}$ or $k_{ji}$ are given by:

$$k_{ij} = k_{ij}(0) \cdot \exp\left(-z_{ij} V / K_B T\right)$$

Where $k_{ij}(0)$ is the value of the rate constant at 0 mV, $z_{ij}$ is the partial charge associated with the transition and $K_B T$ have the same meaning as in Eq.1.

The current as a function of time $t$ and voltage $V$ was calculated as:

$$I(t,V) = \gamma_{ch} \cdot N \cdot (V - V_{rev}) \cdot P_o(t,V) + \gamma_{leak} \cdot (V - V_{rev}^{leak})$$

$\gamma_{ch}$ is the single proton channel conductance, $N$ is the number of channels, $V_{rev}$ is the reversal potential and $P_o$ is the probability of the open state. $\gamma_{leak}$ is the leak conductance and $V_{rev}^{leak}$ is the reversal potential of the leak currents.

The fluorescence was calculated as:

$$F(t,V) = \sum_{i=0}^{n} P_i(t,V) \cdot f_i$$

$f_i$ is the fluorescence of the $i$-th state in arbitrary units.

**Acknowledgements**

We thank Eduardo Guevara for measurements of Anap spectra in different solvents and Manuel Hernández for excellent technical support. We thank Dr. Sebastian Brauchi for the loan of the 405 nm laser. This work was supported by DGAPA-PAPIIT-UNAM grant No.

IN215621. E. S-D is a doctoral student from Programa de Doctorado en Ciencias Bioquímicas-UNAM and was supported by a doctoral thesis scholarship from CONACyT No. 463819 (grantee number: 576613).

## References

1. M. Sasaki, M. Takagi, Y. Okamura, A Voltage Sensor-Domain Protein Is a Voltage-Gated Proton Channel. *Science* **312**, 589–592 (2006).

2. I. S. Ramsey, M. M. Moran, J. A. Chong, D. E. Clapham, A voltage-gated proton-selective channel lacking the pore domain. *Nature* **440**, 1213–1216 (2006).

3. L. Catacuzzeno, F. Franciolini, The 70-year search for the voltage sensing mechanism of ion channels. *The Journal of Physiology*, JP282780 (2022).

4. C. Gonzalez, *et al.*, Voltage sensor of ion channels and enzymes. *Biophys Rev* **4**, 1–15 (2012).

5. J. Ma, *et al.*, The HVCN1 voltage-gated proton channel contributes to pH regulation in canine ventricular myocytes. *The Journal of Physiology* **600**, 2089–2103 (2022).

6. I. S. Ramsey, E. Ruchti, J. S. Kaczmarek, D. E. Clapham, Hv1 proton channels are required for high-level NADPH oxidase-dependent superoxide production during the phagocyte respiratory burst. *Proc. Natl. Acad. Sci. U.S.A.* **106**, 7642–7647 (2009).

7. P. V. Lishko, Y. Kirichok, The role of Hv1 and CatSper channels in sperm activation: Hv1 and CatSper channels in sperm activation. *The Journal of Physiology* **588**, 4667–4672 (2010).

8. R. Eckert, T. Sibaoka, The Flash-Triggering Action Potential of the Luminescent Dinoflagellate Noctiluca. *Journal of General Physiology* **52**, 258–282 (1968).

9. A. R. Taylor, A. Chrachri, G. Wheeler, H. Goddard, C. Brownlee, A Voltage-Gated H+ Channel Underlying pH Homeostasis in Calcifying Coccolithophores. *PLoS Biol* **9**, e1001085 (2011).

10. G. Rangel-Yescas, *et al.*, Discovery and characterization of Hv1-type proton channels in reef-building corals. *eLife* **10**, e69248 (2021).

11. E. Hondares, *et al.*, Enhanced activation of an amino-terminally truncated isoform of the voltage-gated proton channel HVCN1 enriched in malignant B cells. *Proc. Natl. Acad. Sci. U.S.A.* **111**, 18078–18083 (2014).

592 12. Y. Wang, S. J. Li, X. Wu, Y. Che, Q. Li, Clinicopathological and Biological Significance of
593 Human Voltage-gated Proton Channel Hv1 Protein Overexpression in Breast Cancer.
594 *Journal of Biological Chemistry* **287**, 13877–13888 (2012).

595 13. L.-J. Wu, Microglial Voltage-Gated Proton Channel Hv1 in Ischemic Stroke. *Transl. Stroke*
596 *Res.* **5**, 99–108 (2014).

597 14. Y. Yu, *et al.*, Microglial Hv1 proton channels promote white matter injuries after chronic
598 hypoperfusion in mice. *J. Neurochem.* **152**, 350–367 (2020).

599 15. R. Zhao, *et al.*, Role of human Hv1 channels in sperm capacitation and white blood cell
600 respiratory burst established by a designed peptide inhibitor. *Proc. Natl. Acad. Sci. U.S.A.*
601 **115** (2018).

602 16. Q. Zhang, *et al.*, Inhibiting Hv1 channel in peripheral sensory neurons attenuates chronic
603 inflammatory pain and opioid side effects. *Cell Res* **32**, 461–476 (2022).

604 17. B. Musset, *et al.*, Detailed comparison of expressed and native voltage-gated proton
605 channel currents: Voltage-dependent proton channel gating. *The Journal of Physiology*
606 **586**, 2477–2486 (2008).

607 18. H. P. Koch, *et al.*, Multimeric nature of voltage-gated proton channels. *Proc. Natl. Acad.*
608 *Sci. U.S.A.* **105**, 9111–9116 (2008).

609 19. S.-Y. Lee, J. A. Letts, R. MacKinnon, Dimeric subunit stoichiometry of the human voltage-
610 dependent proton channel Hv1. *Proc. Natl. Acad. Sci. U.S.A.* **105**, 7692–7695 (2008).

611 20. F. Tombola, M. H. Ulbrich, E. Y. Isacoff, The Voltage-Gated Proton Channel Hv1 Has Two
612 Pores, Each Controlled by One Voltage Sensor. *Neuron* **58**, 546–556 (2008).

613 21. Q. Li, *et al.*, Resting state of the human proton channel dimer in a lipid bilayer. *Proc. Natl.*
614 *Acad. Sci. U.S.A.* **112** (2015).

615 22. V. V. Cherny, V. S. Markin, T. E. DeCoursey, The voltage-activated hydrogen ion
616 conductance in rat alveolar epithelial cells is determined by the pH gradient. *The Journal of*
617 *general physiology* **105**, 861–896 (1995).

618 23. S. M. E. Smith, *et al.*, Voltage-gated proton channel in a dinoflagellate. *Proc. Natl. Acad.*
619 *Sci. U.S.A.* **108**, 18162–18167 (2011).

620 24. C. Zhao, F. Tombola, Voltage-gated proton channels from fungi highlight role of peripheral
621 regions in channel activation. *Commun Biol* **4**, 261 (2021).

622 25. T. M. Schladt, T. K. Berger, Voltage and pH difference across the membrane control the S4
623 voltage-sensor motion of the Hv1 proton channel. *Sci Rep* **10**, 21293 (2020).

624 26. E. M. Carmona, *et al.*, The voltage sensor is responsible for ΔpH dependence in $H_v1$
625 channels. *Proc. Natl. Acad. Sci. U.S.A.* **118**, e2025556118 (2021).

626 27. E. M. Carmona, *et al.*, Gating charge displacement in a monomeric voltage-gated proton ($H_v1$)
627 channel. *Proc. Natl. Acad. Sci. U.S.A.* **115**, 9240–9245 (2018).

628 28. V. De La Rosa, I. S. Ramsey, Gating Currents in the Hv1 Proton Channel. *Biophysical Journal*
629 **114**, 2844–2854 (2018).

630 29. J. Kusch, G. Zifarelli, Patch-Clamp Fluorometry: Electrophysiology meets Fluorescence.
631 *Biophysical Journal* **106**, 1250–1257 (2014).

632 30. L. Mony, T. K. Berger, E. Y. Isacoff, A specialized molecular motion opens the Hv1 voltage-
633 gated proton channel. *Nat Struct Mol Biol* **22**, 283–290 (2015).

634 31. F. Qiu, S. Rebolledo, C. Gonzalez, H. P. Larsson, Subunit Interactions during Cooperative
635 Opening of Voltage-Gated Proton Channels. *Neuron* **77**, 288–298 (2013).

636 32. A. Chatterjee, J. Guo, H. S. Lee, P. G. Schultz, A Genetically Encoded Fluorescent Probe in
637 Mammalian Cells. *J. Am. Chem. Soc.* **135**, 12540–12543 (2013).

638 33. M. C. Puljung, "ANAP: A versatile, fluorescent probe of ion channel gating and regulation"
639 in *Methods in Enzymology*, (Elsevier, 2021), pp. 49–84.

640 34. T. Kalstrup, R. Blunck, Dynamics of internal pore opening in $K_V$ channels probed by a
641 fluorescent unnatural amino acid. *Proc. Natl. Acad. Sci. U.S.A.* **110**, 8272–8277 (2013).

642 35. S. E. Gordon, M. Munari, W. N. Zagotta, Visualizing conformational dynamics of proteins in
643 solution and at the cell membrane. *eLife* **7**, e37248 (2018).

644 36. V. De-la-Rosa, E. Suárez-Delgado, G. E. Rangel-Yescas, L. D. Islas, Currents through Hv1
645 channels deplete protons in their vicinity. *Journal of General Physiology* **147**, 127–136
646 (2016).

647 37. L. Zhang, K. Bellve, K. Fogarty, W. R. Kobertz, Fluorescent Visualization of Cellular Proton
648 Fluxes. *Cell Chemical Biology* **23**, 1449–1457 (2016).

649 38. M. Vaid, T. W. Claydon, S. Rezazadeh, D. Fedida, Voltage Clamp Fluorimetry Reveals a
650 Novel Outer Pore Instability in a Mammalian Voltage-gated Potassium Channel. *Journal of*
651 *General Physiology* **132**, 209–222 (2008).

652 39. A. Cha, F. Bezanilla, Structural Implications of Fluorescence Quenching in the Shaker K+
653 Channel. *Journal of General Physiology* **112**, 391–408 (1998).

654 40. A. S. Klymchenko, Solvatochromic and Fluorogenic Dyes as Environment-Sensitive Probes:
655 Design and Biological Applications. *Acc. Chem. Res.* **50**, 366–375 (2017).

656 41. A. L. Randolph, Y. Mokrab, A. L. Bennett, M. S. Sansom, I. S. Ramsey, Proton currents
657 constrain structural models of voltage sensor activation. *eLife* **5**, e18017 (2016).

658 42. X. Tao, A. Lee, W. Limapichat, D. A. Dougherty, R. MacKinnon, A Gating Charge Transfer
659 Center in Voltage Sensors. *Science* **328**, 67–73 (2010).

660 43. L. Hong, M. M. Pathak, I. H. Kim, D. Ta, F. Tombola, Voltage-sensing domain of voltage-
661 gated proton channel Hv1 shares mechanism of block with pore domains. *Neuron* **77**, 274–
662 287 (2013).

663 44. P. Thomas, T. G. Smart, HEK293 cell line: A vehicle for the expression of recombinant
664 proteins. *Journal of Pharmacological and Toxicological Methods* **51**, 187–200 (2005).

665 45. C. A. Villalba-Galea, Hv1 proton channel opening is preceded by a voltage-independent
666 transition. *Biophysical journal* **107**, 1564–1572 (2014).

667 46. E. Stefani, *et al.*, Voltage-controlled gating in a large conductance $Ca^{2+}$-sensitive $K^{+}$
668 channel (hslo). *Proc. Natl. Acad. Sci. U.S.A.* **94**, 5427–5431 (1997).

669 47. V. V. Cherny, *et al.*, Tryptophan 207 is crucial to the unique properties of the human
670 voltage-gated proton channel, hHV1. *Journal of General Physiology* **146**, 343–356 (2015).

671 48. T. Kalstrup, R. Blunck, S4–S5 linker movement during activation and inactivation in
672 voltage-gated $K^{+}$ channels. *Proc. Natl. Acad. Sci. U.S.A.* **115** (2018).

673 49. G. Dai, T. K. Aman, F. DiMaio, W. N. Zagotta, The HCN channel voltage sensor undergoes a
674 large downward motion during hyperpolarization. *Nat Struct Mol Biol* **26**, 686–694 (2019).

675 50. I. S. Ramsey, *et al.*, An aqueous H+ permeation pathway in the voltage-gated proton
676 channel Hv1. *Nat Struct Mol Biol* **17**, 869–875 (2010).

677 51. A. Cha, F. Bezanilla, Characterizing Voltage-Dependent Conformational Changes in the K
678 Channel with Fluorescence. *Neuron* **19**, 1127–1140 (1997).

679 52. L. Zheng, U. Baumann, J.-L. Reymond, An efficient one-step site-directed and site-
680 saturation mutagenesis protocol. *Nucleic Acids Research* **32**, e115 (2004).

681 53. B. Munteanu, M. Braun, K. Boonrod, Improvement of PCR reaction conditions for site-
682 directed mutagenesis of big plasmids. *J. Zhejiang Univ. Sci. B* **13**, 244–247 (2012).

683 54. A. D. Edelstein, *et al.*, Advanced methods of microscope control using μManager software.
684 *J Biol Methods* **1**, e10 (2014).

685

686

687 **Figures and Figure legends**

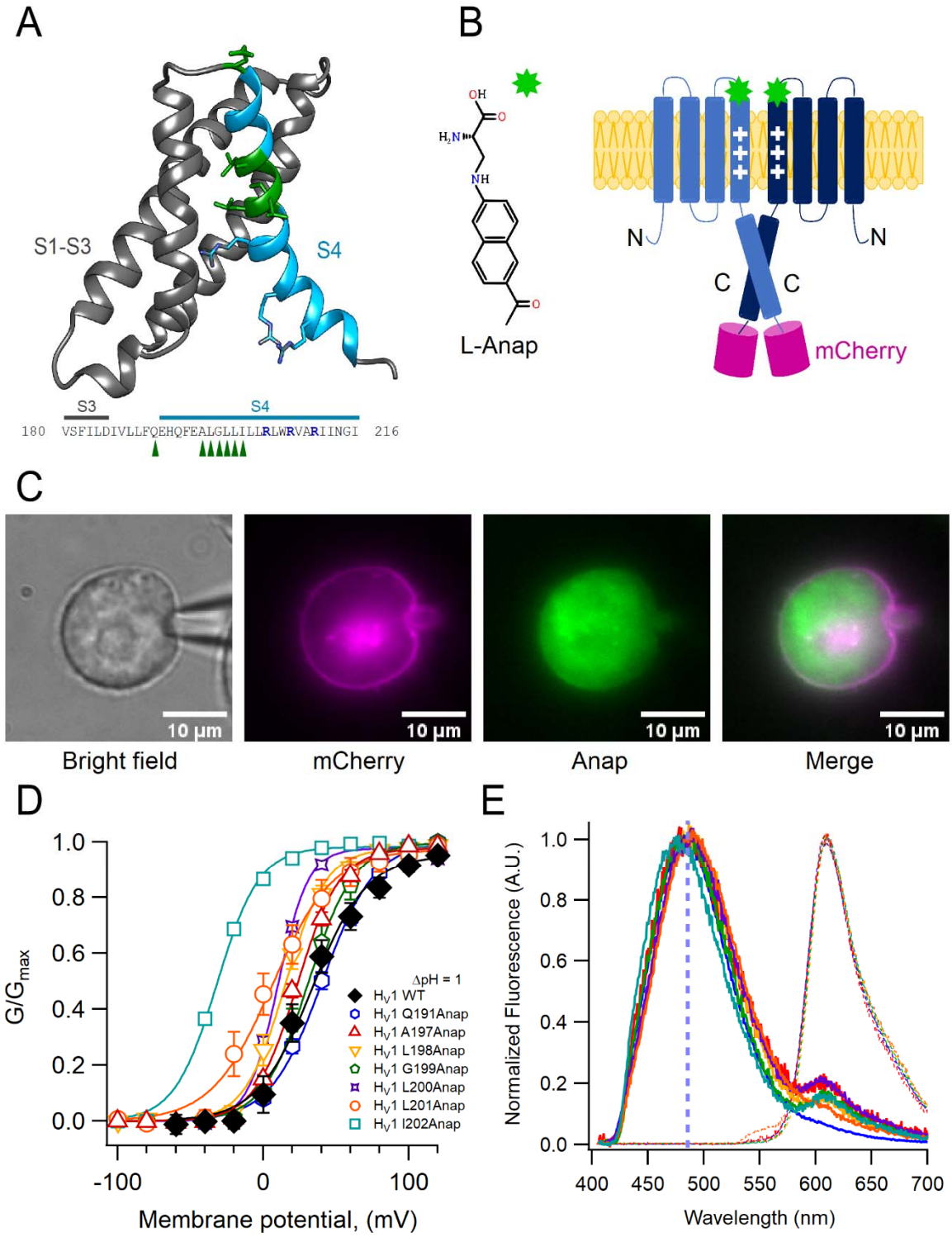


Figure 1

688

689 **Figure 1.** Anap as a fluorescent probe in $hH_V1$. A) Ribbon representation of
690 transmembrane segments S1-S4 of closed $hH_V1$ based on the model of Randolph et al. (41).
691 S1-S3 are in grey whereas S4 is in light blue. S4 positively charged arginine residues are
692 shown as cyan sticks, whereas the residues where Anap was incorporated individually in
693 the S4 segment are depicted as green sticks and with green arrow heads in the S3-S4
694 sequence below; positively charged arginine residues are indicated in marine blue. B)
695 Structure of non-canonical amino acid Anap (left), and a schematic representation (right)
696 that shows the incorporation of Anap (green star) into the $hH_V1$ dimer expressed in
697 HEK293 cells. An mCherry fluorescent protein (magenta cylinder) was fused to the C-
698 terminal end of $hH_V1$ as an Anap incorporation reporter. C) Images of a representative
699 Patch-clamp Fluorometry (PCF) experiment, showing the voltage-clamped cell and the co-
700 localization of Anap and mCherry fluorescence in the cell membrane for Anap incorporated
701 at position Q191 of $hH_V1$. D) G-V curves obtained from currents produced by each $hH_V1$
702 mutant rescued by Anap incorporation. All G-V s were obtained at ΔpH=1 and compared
703 with $hH_V1$ WT. Continuous lines are the fit of the conductance data to equation 1; fit
704 parameters are summarized in Supplemental table I. The incorporation of Anap at the I202
705 site sifts the G-V ~65 mV to more negative potentials. Data shown are mean ± s.e.m. E)
706 Normalized mean emission spectrum of Anap (continuous lines) and mCherry (dashed
707 lines) at each incorporation site (color code from D). Q191(n=15); A197(n=10); L198(n=3);
708 G199(n=5); L200(n=1); L201(n=4); I202(n=5). The vertical blue line indicates the peak
709 emission of Anap in water (486 nm). A second emission peak can be distinguished in every
710 position inside S4 where Anap was incorporated, except Q191Anap. This peak is located
711 around 610 nm which coincides with the peak emission of mCherry.
712

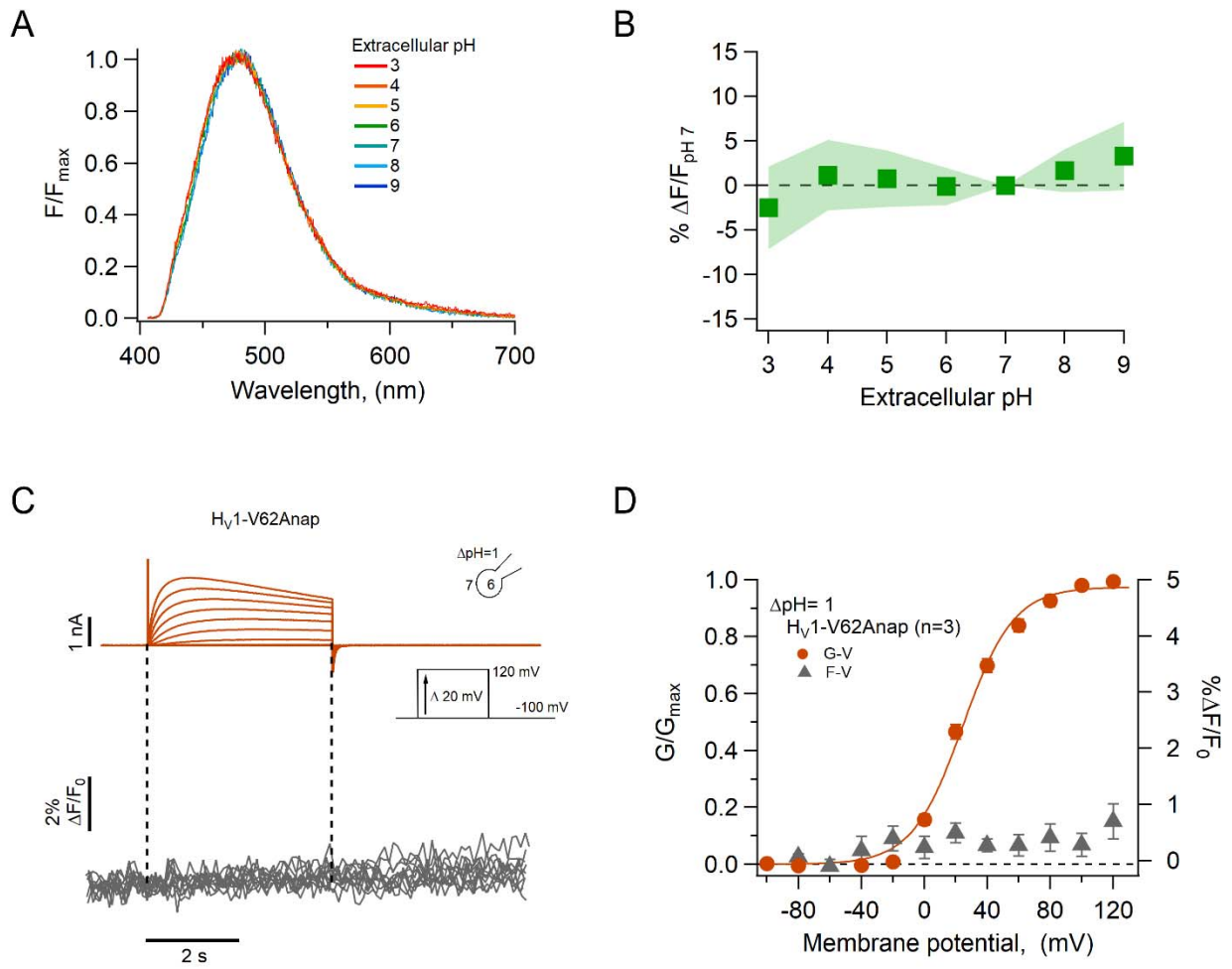


Figure 2

**Figure 2.** The fluorescence of incorporated Anap is stable to external acidity and local pH changes. A) Mean spectra of Anap fluorescence in the $hH_V1$-Q191Anap mutant at each external pH tested ($pH_o$). The emission peak of spectra of Anap remained inside the wavelength range of 475-480 nm. B) Percentage of fluorescence intensity change normalized to fluorescence at $pH_o$ 7 in $hH_V1$-Q191Anap mutant (n=13). The intensity was measured from the peak of emission spectra. C) Representative PCF experiments with the $hH_V1$-V62Anap mutant. Currents (upper panel, orange traces) and fluorescent signal (lower panel, gray traces) were elicited in response to voltage pulses from -100 mV to 120 mV in steps of 20 mV. D) F-V and G-V relationships from the experiments shown in C. Relative fluorescence changes at the end of voltage test pulses are shown in gray triangles, and conductance is shown in orange circles. The orange continuous line is the fit to

equation 1 of G-V data (fit parameters: $V_{0.5}$ = 24.4 ± 1.6 mV; q = 1.5 ± 0.1 $e_0$). Data in B and D are Mean ± s.e.m.

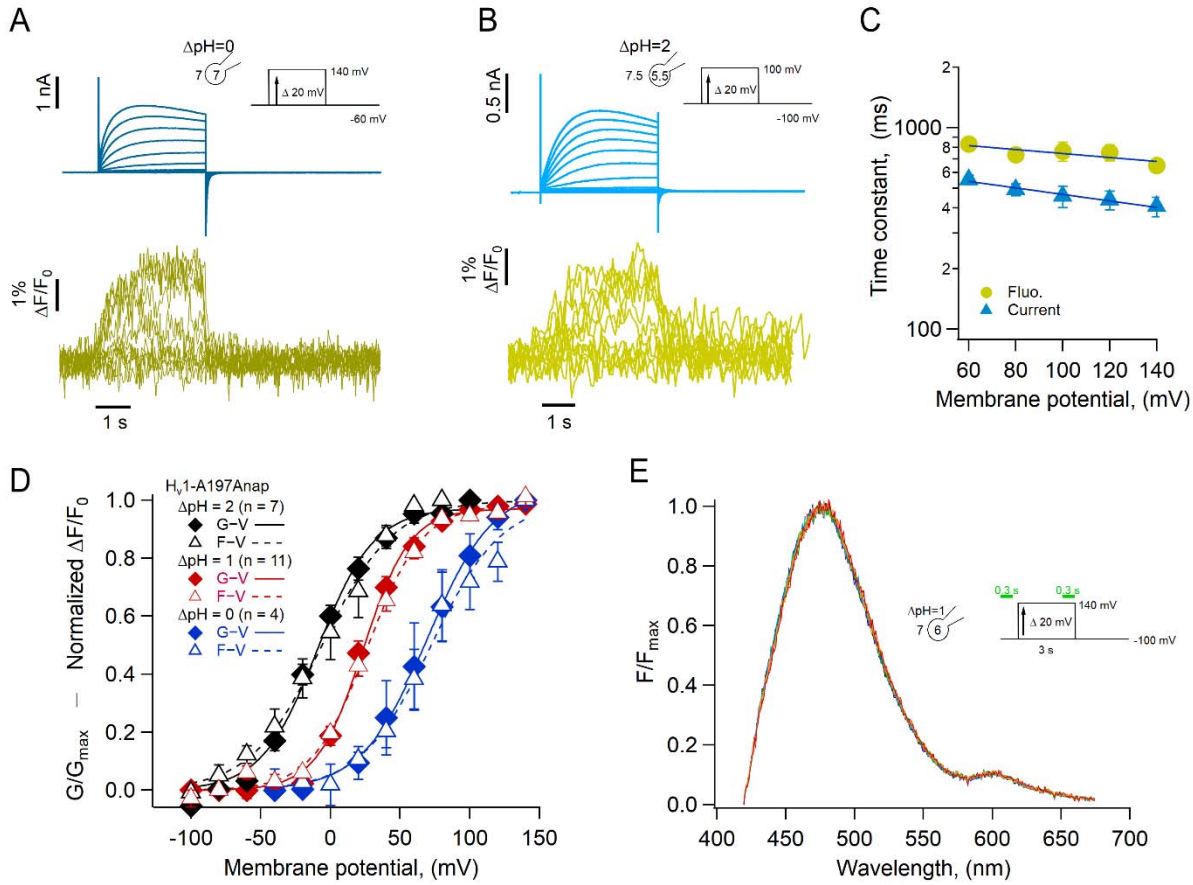


Figure 3

**Figure 3.** Anap incorporation in position A197 reveals that the movement of S4 is modulated by ΔpH. A-B) Representative PCF experiment with A197Anap at ΔpH=0 and ΔpH=2, respectively. Proton current families (upper panels) are shown in blue traces and fluorescent Anap signal (lower panel) in lemon traces. C) Activation time constant of current (blue) and fluorescent (lemon) signals at ΔpH=0 obtained by fitting Eq. 3. The dark blue curve shows the exponential fit to Eq. 4. The fit parameters were: $\tau(0)$ = 935 ms and $q$ = -0.06 $e_0$ for fluorescence and 678 ms and -0.09 $e_0$ for current. D) F-V (empty triangles) and G-V (filled diamonds) curves and different ΔpH values (ΔpH=0 in blue; ΔpH=1 in red; ΔpH=2 in black). The data were fit to equation 1(G-V, continuous curves; F-V, discontinuous curves) with the following parameters: ΔpH=0; F-V: $V_{0.5}$ = 72.3 ± 6 mV; q = 1.0 ± 0.1 $e_0$. G-V:

$V_{0.5}$ = 69.6 ± 1.5 mV; q = 1.1 ± 0.1 $e_0$. ΔpH =1; F-V: $V_{0.5}$ = 26.6 ± 1.5 mV; q = 1.3± 0.1 $e_0$. G-V: $V_{0.5}$ = 23.4 ± 1.3 mV; q = 1.5 ± 0.1 $e_0$. ΔpH = 2; F-V: $V_{0.5}$ = -6.1 ± 1.8 mV; q = 1.0 ± 0.1 $e_0$. G-V: $V_{0.5}$ = -9.2 ± 2.3 mV; q = 1.2 ± 2.4 $e_0$. E) Normalized spectra of Anap in A197Anap mutant obtained in steady-state (300 ms at the end of holding potential and the end of the test pulse, green bars in the inset) in response to different voltages (color code indicates the test pulse in mV: purple, -60; dark blue, -40; light blue, 20; cyan, 0; light green, 20; dark green, 40; olive, 60; yellow, 80; orange, 100; dark red, 120; red, 140). Data shown in C and D are mean ± s.e.m.

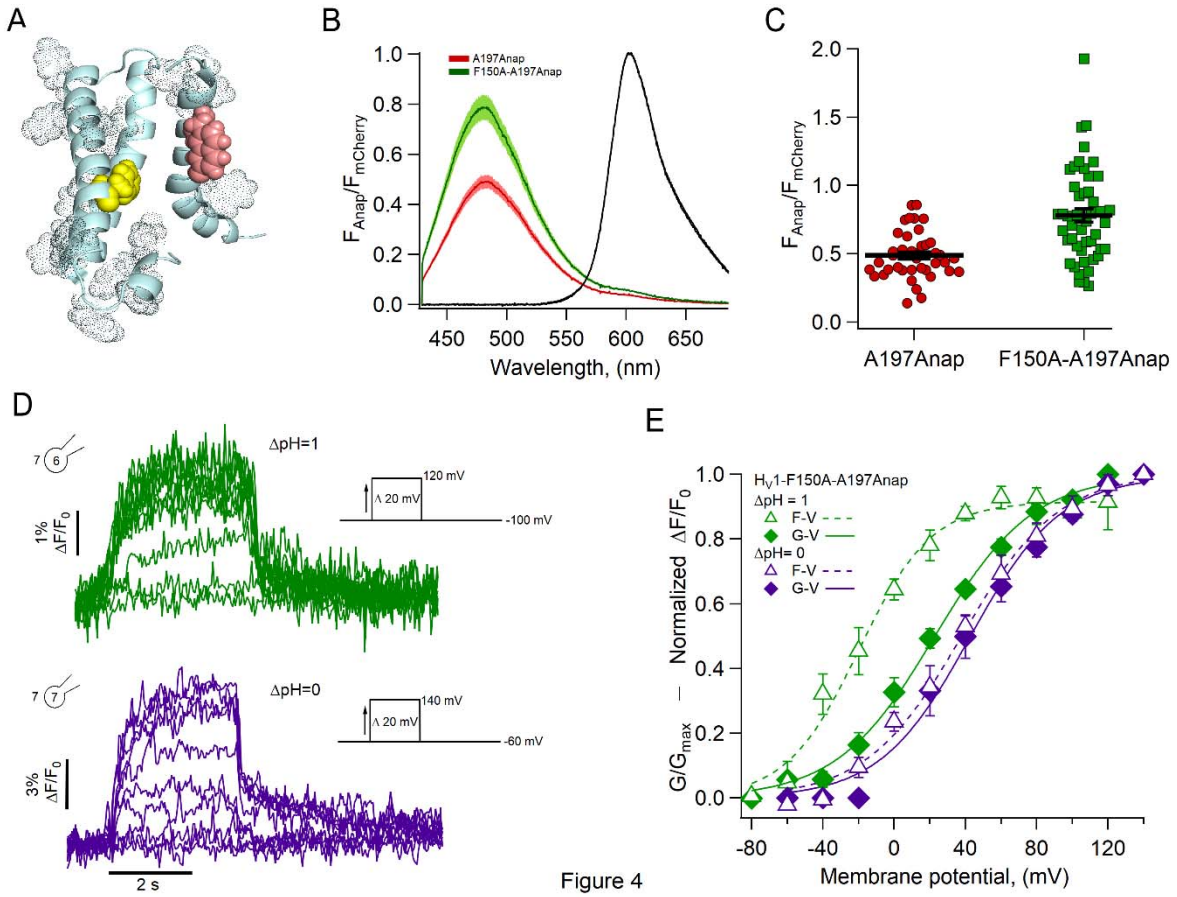


Figure 4

**Figure 4.** The charge transfer center (F150) is an Anap quencher. A) Cartoon showing the presence of aromatic residues in $hH_V1$ (rendered as space-filling dots, main chain in light blue, S3 was removed for illustration). F150 in yellow and Anap in pink. B) Averages of spectra of Anap incorporated in both mutants ($H_V1$-A197Anap, red; $H_V1$-F150A-A197Anap, green) normalized to the fluorescence of mCherry (black). The double mutant's brightness is approximately 60% higher. Shadows represent s.e.m. C) Comparison of the intensity of the emission spectrum peak of Anap normalized to the intensity of the fluorescent protein mCherry between the mutant $H_V1$-A197Anap-Cherry (0.49 ± 0.03) and double mutant $H_V1$-F150A-A197Anap-Cherry (0.79 ± 0.05), taken at 48 hours post-transfection. Each point indicates an individual spectrum measured from a single cell; n = 41 and 49, respectively. Black horizontal lines are the mean ± s.e.m. T-test value $p < 0.001$. D) Representative fluorescence traces from PCF experiments of the double mutant $H_V1$-F150A-A197Anap at ΔpH=1 (upper panel) and ΔpH=0 (lower panel). E) Comparison of G-V (diamonds) and F-V

765 (triangles) relationship between both ΔpH conditions (ΔpH=1 in green; ΔpH=0 in purple)
766 of the double mutant $H_V1$-F150A-A197Anap. F-V curve of $H_V1$-F150A-A197Anap at ΔpH=0
767 is shifted negatively around 58 mV compared to ΔpH=1. Boltzmann fit parameters of $H_V1$-
768 F150A-A197Anap were: ΔpH=1 F-V: $V_{0.5}$=-19.8 ± 2.7 mV; q =1.2 ± 0.1 $e_0$; G-V: $V_{0.5}$ = 22.7 ±
769 2.3 mV; q = 0.9 ± 0.1 $e_0$. ΔpH=0 F-V: $V_{0.5}$=38.0 ± 3.0 mV; q =0.9 ± 0.1 $e_0$; G-V: $V_{0.5}$ = 42.6 ±
770 3.8 mV; q = 1.0 ± 0.1 $e_0$. Data shown in B, C and E are mean ± s.e.m.
771

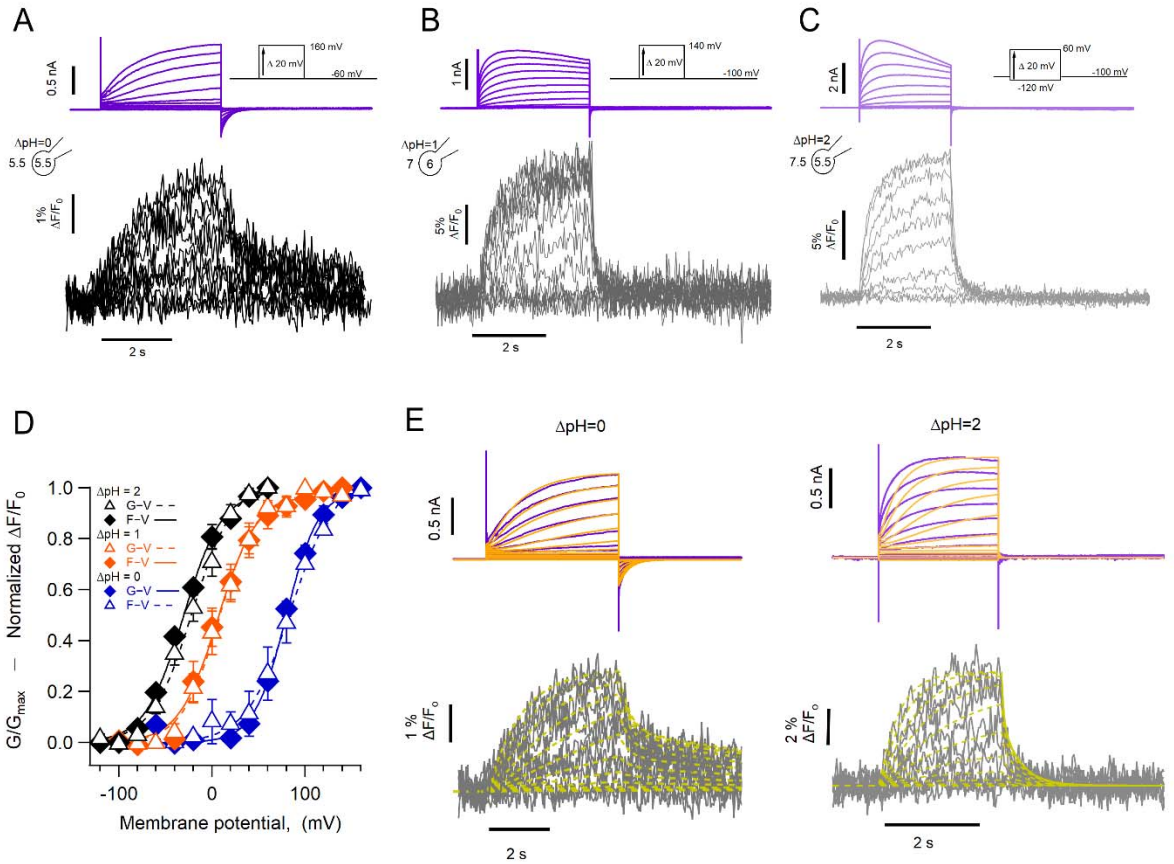


Figure 5

**Figure 5**. The kinetics of fluorescent signal during deactivation is strongly modulated by pH. Representative PCF experiments with the $hH_V1$-L201Anap mutant at A) ΔpH=0 [$5.5_{int}$-$5.5_{ext}$]. B) ΔpH=1, and C) ΔpH=2. Current families are shown in the upper panel (purple traces) and fluorescent signals in the lower panel (black and gray traces). D) G-V (filled diamonds) and F-V (empty triangles) relationships at ΔpH=0 (purple markers, n = 3), ΔpH=1 (orange markers, n=4) and ΔpH=2 (black markers, n=5) of mutant $hH_V1$-L201Anap. Data are mean ± s.e.m. Note that the difference between the activation at ΔpH=1 and ΔpH=0 is around 77 mV/ΔpH unit. Boltzmann fit parameters: ΔpH=0, F-V; $V_{0.5}$= 84.6 ± 2.1 mV, q =1.0 $e_0$ ± 0.1. G-V; $V_{0.5}$= 79.7 ± 1.8 mV, q = 1.4 ± 0.1 $e_0$. ΔpH =1, F-V; $V_{0.5}$= 7.7 ± 1.6 mV, q =1.2 ± 0.1 $e_0$. G-V: $V_{0.5}$= 6.3 ± 2.2 mV; q = 1.2 ± 0.1 $e_0$. ΔpH = 2, F-V: $V_{0.5}$= -21.1 ± 2.3 mV; q =1.1 ± 0.1 $e_0$. G-V: $V_{0.5}$= -30.7 ± 1.9 mV; q = 1.2 ± 0.1 $e_0$. E) Comparison of the current and fluorescence at two values of ΔpH with the predictions of the sequential activation model in Scheme I. Experimental current and fluorescence traces are color coded as in A). Simulated

787 current traces are orange and fluorescence traces are lemon. Simulation parameters can be
788 found in Supplementary Table II.
789

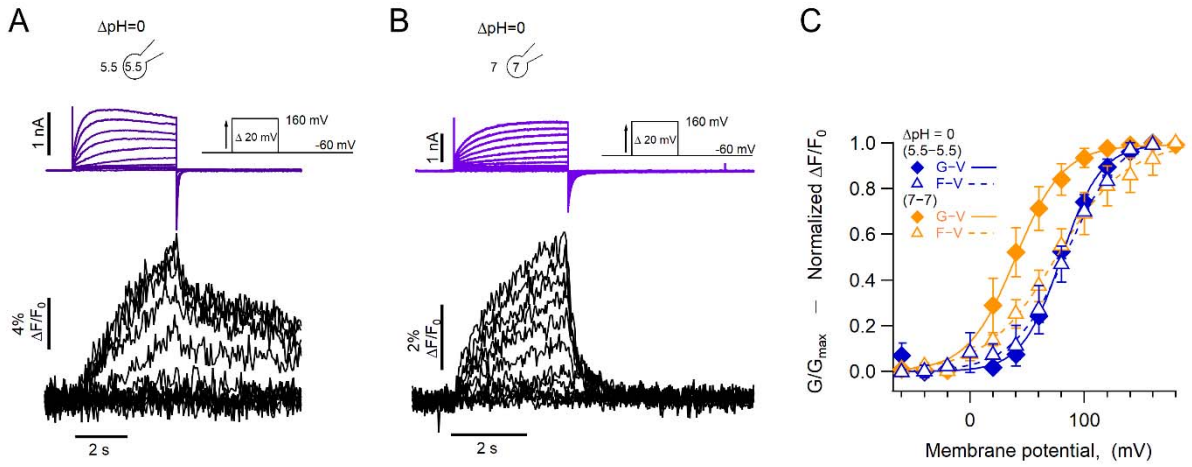


Figure 6

**Figure 6.** Absolute pH values are gating determinants in $hH_V1$. A) Representative PCF experiment at ΔpH=0 ($5.5_o$-$5.5_i$). Currents are purple and fluorescence black. B) Similar experiment to A) with ΔpH=0 ($7_o$-$7_i$). Current and fluorescence traces color coded as in A). C) G-V (filled diamonds) and F-V (empty triangles) curves at ΔpH=0 but with different absolute pH values ($pH_o/pH_i$ =5.5/5.5 in blue; $pH_o/pH_i$ =7/7 in orange, n= 4). Boltzmann fit parameters were $pH_o/pH_i$ =7/7 F-V: $V_{0.5}$= 75.3 ± 2.2 mV; q =0.8 ± 0.04 $e_0$. G-V: $V_{0.5}$= 39.6 ± 1.3 mV; q = 1.2 ± 0.1 $e_0$. $pH_o/pH_i$ =5.5/5.5 F-V: $V_{0.5}$= 84.6 ± 2.1 mV; q =1.0 $e_0$ ± 0.1. G-V: $V_{0.5}$= 79.7 ± 1.8 mV; q = 1.4 ± 0.1 $e_0$. Data are mean ± s.e.m.